APL Materials

RESEARCH ARTICLE | DECEMBER 04 2023

Large voltage-controlled magnetic anisotropy effect in magnetic tunnel junctions prepared by deposition at cryogenic temperatures

Takayuki Nozaki ; Tomohiro Ichinose ; Jun Uzuhashi ; Tatsuya Yamamoto ; Makoto Konoto ; Kay Yakushiji ; Tadakatsu Ohkubo ; Shinji Yuasa

APL Mater. 11, 121106 (2023)
https://doi.org/10.1063/5.0176263

Large voltage-controlled magnetic anisotropy effect in magnetic tunnel junctions prepared by deposition at cryogenic temperatures

Cite as: APL Mater. 11, 121106 (2023); doi: 10.1063/5.0176263
Submitted: 12 September 2023 • Accepted: 8 November 2023 •
Published Online: 4 December 2023

Takayuki Nozaki,[1,a)] Tomohiro Ichinose,[1] Jun Uzuhashi,[2] Tatsuya Yamamoto,[1] Makoto Konoto,[1] Kay Yakushiji,[1] Tadakatsu Ohkubo,[2] and Shinji Yuasa[1]

AFFILIATIONS

[1] Research Center for Emerging Computing Technologies, National Institute of Advanced Industrial Science and Technology (AIST), Tsukuba, Ibaraki 305-8568, Japan
[2] Research Center for Magnetic and Spintronic Materials, National Institute for Materials Science (NIMS), Tsukuba, Ibaraki 305-0047, Japan

[a)] **Author to whom correspondence should be addressed:** nozaki-t@aist.go.jp

ABSTRACT

We investigated the influence of the buffer material and a cryogenic temperature deposition process on the voltage-controlled magnetic anisotropy (VCMA) effect for an ultrathin CoFeB layer in bottom-free type MgO-based magnetic tunnel junctions prepared by a mass production sputtering process. We used Ta and TaB buffers and compared the differences between them. The TaB buffer enabled us to form a flat and less-contaminated CoFeB/MgO interface by suppressing the diffusion of Ta with maintaining a stable amorphous phase. Furthermore, the introduction of cryogenic temperature deposition for the ultrathin CoFeB layer on the TaB buffer improved the efficiency of the VCMA effect and its annealing tolerance. Combining this with interface engineering employing an Ir layer for doping and a CoFe termination layer, a large VCMA coefficient of −138 ± 3 fJ/Vm was achieved. The developed techniques for the growth of ultrathin ferromagnet and oxide thin films using cryogenic temperature deposition will contribute to the development of high-performance spintronic devices, such as voltage-controlled magnetoresistive random access memories.

I. INTRODUCTION

Magnetoresistive random access memories (MRAMs) employing MgO-based magnetic tunnel junctions (MTJs) have the potential to be ideal nonvolatile working memories.[1,2] Spin transfer torque (STT)-based embedded MRAMs, in particular, are endeavoring to replace NOR flash memories, EEPROMs, and SRAMs. One of the most important technical challenges for MRAMs, at present, is to reduce the operating energy, i.e., by developing new technologies to control the magnetization direction more efficiently because the high operating energy prevents MRAMs from being applied to a wide range of memory hierarchies. Latest STT writing achieved the low writing energy of the order of 45 fJ/bit;[3] however, this is still higher than that of SRAMs, which are made up of several MOSFETs operated by an electric field. To employ electric-field operation in MRAM technology, the voltage-controlled magnetic anisotropy (VCMA) effect has been investigated as an energy-efficient approach for writing information to voltage-controlled (VC) MRAMs.[4–6] The VCMA effect was first demonstrated in a thin FePt(Pd) film immersed in a liquid electrolyte[7] and then successfully introduced into a MgO-based all solid state structure even in MgO-MTJ devices.[8,9] There are several mechanisms that have been proposed to explain the physical origin of the purely electronic VCMA effect, for example, carrier-mediated modification of the electronic structure[10–12] and an electric-field-induced change in the magnetic dipole[13] at the interface between the ultrathin ferromagnet and the tunneling barrier. The interfacial perpendicular magnetic anisotropy (PMA) can be manipulated by applying a bias voltage, and in most cases, the PMA changes linearly as a function of the applied electric field. The slope of the linear relationship is defined as the VCMA

coefficient with the unit of J/Vm. Although the VCMA effect can induce a transition of the magnetic easy axis between the out-of-plane and in-plane directions through a modification of the height of the magnetic energy barrier, bi-stable switching cannot be induced just by applying a static voltage because the electric-field does not break the time-reversal symmetry. However, the high speed response of the VCMA effect makes it possible to induce precessional magnetization dynamics by applying a short voltage pulse under a bias magnetic field.[14–18] Employing this process, bi-stable dynamic switching on a sub-nanosecond time scale has been demonstrated with ultra-low writing energy (<10 fJ/bit).[19,20]

For the development of VC-MRAMs, an improvement in the VCMA coefficient is needed in order to ensure scalability.[4,17] The data retention of a magnetic bit is determined by the thermal stability factor, $\Delta = K_{PMA}V/k_BT$, where K_{PMA} and V are the effective PMA energy density and the volume of the free layer, respectively, k_B is the Boltzmann constant, and T is the temperature. In order to maintain sufficient Δ for smaller elements, i.e., larger memory capacity, higher K_{PMA} is required. For voltage-induced dynamic magnetization switching, we need to make K_{PMA} zero during the precessional switching process; therefore, a larger VCMA coefficient is required as the element size is scaled down. For example, assuming a MTJ of 30 nm diameter with Δ = 60 and a switching electric-field amplitude of 1 V/nm, a VCMA coefficient with an absolute value of about 300 fJ/Vm is required.[4] A high Δ and a high VCMA coefficient are also crucial for realizing a practical low write error rate by suppressing the influence of thermal fluctuations during the switching process.[4,17,21]

Several experimental approaches have been proposed to enhance the VCMA effect, for example, controlling the interfacial oxidation state,[22,23] optimizing the buffer and capping materials,[24–31] and introducing high-k dielectric materials.[32,33] One of the most effective approaches is the introduction of a heavy metal material that has large spin–orbit interactions in the free layer, such as interface engineering using an Ir layer for doping.[34–37] The proximity-induced magnetism of Ir dispersed in an ultrathin Fe layer brings about an improvement in the VCMA effect. Highly efficient VCMA coefficients exceeding −300 fJ/Vm have been demonstrated in epitaxial MTJs with high speed response. On the other hand, the VCMA coefficient in polycrystalline MTJs is still limited to about −100 fJ/Vm.[22,24,27] It is particularly difficult to realize a high VCMA coefficient in a MTJ structure with a bottom free layer mainly because of the diffusion of the buffer materials, although the bottom free layer structure is advantageous in regard to the introduction of interface engineering, such as heavy metal doping, with keeping flat interface compared to that of the top free structure.

In this work, we systematically investigated the influence of the buffer material on the magnetic anisotropy, tunneling magnetoresistance (TMR), and the VCMA properties in CoFeB/MgO MTJs with a bottom free layer prepared by a mass production sputtering process. Moreover, we examined the effect of deposition of the ultrathin CoFeB layer at cryogenic temperatures on the above properties. The introduction of an amorphous TaB buffer and an ultrathin CoFeB layer deposited at cryogenic temperatures led to improvements in the PMA, TMR, and VCMA properties. The microstructural analysis revealed that the stable amorphous phase of the TaB buffer was effective in suppressing Ta diffusion into the ultrathin CoFeB layer and contributed to the formation of a flat and less-contaminated CoFeB/MgO interface. Furthermore, combining with the cryogenic temperature deposition and interface engineering employing an Ir layer with a CoFe termination layer, we achieved a large VCMA coefficient of −138 ± 3 fJ/Vm.

II. MATERIALS AND METHODS

Multilayer structures consisting of Ta(5 nm)/Ru(5 nm)/Ta(5 nm)/Ru(5 nm)/Ta or $Ta_{50}B_{50}$(5 nm)/$Co_{40}Fe_{40}B_{20}$(t_{CFB})/Ir(t_{Ir})/$Co_{50}Fe_{50}$ termination layer (0.1 nm)/MgO(t_{MgO} = 2.1 nm)/$Co_{40}Fe_{40}B_{20}$(3 nm)/Ta(3 nm)/Ru(10 nm) were prepared on ϕ300 mm thermally oxidized Si wafers using a mass production sputtering system (EXIM, Tokyo Electron Ltd.) as shown in Fig. 1(a). Hereafter, $Ta_{50}B_{50}$, $Co_{40}Fe_{40}B_{20}$, and $Co_{50}Fe_{50}$ are referred to as TaB, CoFeB, and CoFe, respectively, for simplicity. The sputtering system has seven chambers, each with four cathodes. One of the chambers also has a stage cooled by a He refrigerator, which makes it possible to deposit films at cryogenic temperatures with wafer rotation [Fig. 1(b)]. In our recent work, cryogenic temperature deposition was found to be effective for improving the PMA, TMR, VCMA, and magnetic damping properties of a top free ultrathin CoFeB layer deposited on a MgO tunneling barrier on account of the less-intermixed interface.[38,39] In this experiment, we adopted cryogenic temperature (−173 °C) deposition for the CoFeB bottom free layer, the CoFe termination layer, and the top CoFeB reference layer (see Fig. 1). The magnetic easy axis of the bottom free layer was designed to be in the out-of-plane direction, while that of the top reference layer was in the in-plane direction. This orthogonally magnetized MTJ is advantageous for evaluating the effective K_{PMA} energy of the free layer and the VCMA coefficient through TMR measurements, as discussed later. MTJ devices with cross-sectional areas of 2 × 6 μm^2 were fabricated by conventional optical lithography, ion-milling, and a lift-off process. *Ex situ* annealing was performed after the microfabrication process in a vacuum furnace with temperatures T_{an} ranging from 200 to 350 °C. The TMR curves were measured by a direct-current two-probe method under the application of an in-plane magnetic field. The saturation magnetization

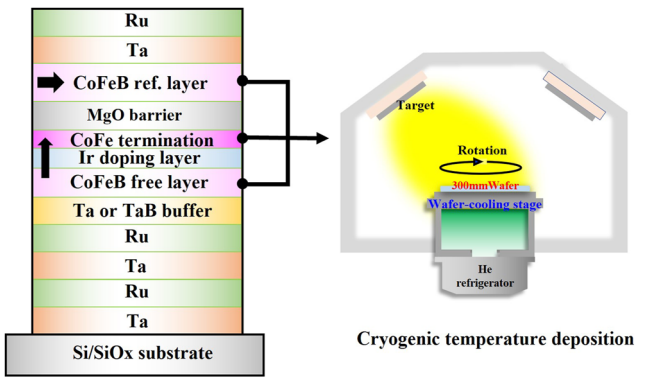

FIG. 1. Schematic illustration of magnetic tunnel junctions prepared on Φ300 mm thermally oxidized Si wafers. The CoFeB and CoFe layers were deposited using a cryogenic temperature deposition process.

of the free layer was independently evaluated by vibrating sample magnetometry (VSM). Microstructural analysis was performed by cross-sectional scanning transmission electron microscopy (STEM), nanobeam electron diffraction (NBED), energy dispersive x-ray spectroscopy (EDS), and electron energy-loss spectroscopy (EELS) using a FEI Titan G2 80-200. Thin foil specimens were prepared by a lift-out technique using a FEI Helios 5UX focused ion beam (FIB). All measurements in this study were conducted at room temperature.

III. RESULTS AND DISCUSSION

A. Influence of the buffer material and the CoFeB deposition temperature on the PMA, TMR, and VCMA properties

We first compared the PMA, TMR, and VCMA properties for MTJs with an ultrathin CoFeB layer grown on a Ta or TaB buffer. For this experiment, a single 0.9 nm-thick CoFeB layer was used as the bottom free layer, i.e., an Ir/CoFe bilayer was not inserted. Figures 2(a) and 2(c) show the bias voltage (V_{bias}) dependence of the TMR curves measured under the application of an in-plane magnetic field (H_{ex}) for orthogonally magnetized MTJs with the (a) Ta buffer and (c) TaB buffer, respectively. In both cases, the CoFeB layer was deposited with the temperature of the stage at −173 °C and the post-annealing temperature was fixed at T_{an} = 350 °C. The vertical axis is normalized by the maximum resistance (at H_{ex} = 0 A/m) and minimum resistance (at H_{ex} = 500 kA/m) in order to avoid the influence of the bias voltage dependence of the tunneling resistance. The sign of V_{bias} is defined with respect to the top CoFeB layer, i.e., a positive (negative) bias induces electron accumulation (depletion) at the interface between the CoFeB bottom free layer and the MgO tunneling barrier. Magnetization of the perpendicularly magnetized free layer is tilted into the direction of the film plane by the application of the in-plane magnetic field, while that of the reference layer is maintained in the film plane as illustrated in Fig. 2(a). Therefore, saturation of the tunneling resistance reflects the magnetization process of the free layer in the magnetic hard axis direction. Since the tunneling conductance depends on the relative angle between the free and reference layers, the ratio of the in-plane magnetization component of the free layer, $M_{in\text{-}plane}$, to its saturation magnetization, M_S, can be calculated from the TMR curves. Then, the effective perpendicular magnetic anisotropy energy, K_{PMA}, can be evaluated from the $M_{in\text{-}plane}$ (H) area by combining it with the M_S value obtained from independent VSM measurements (see Ref. 32 for the detailed evaluation process). Figures 2(b) and 2(d) show the applied electric field, V_{bias}/t_{MgO}, dependence of $K_{PMA}t_{free}$ for structures with the (b) Ta buffer and (d) TaB buffer, respectively. Here, $t_{free} = t_{CFB} - t_d$, where t_d is the magnetic dead layer thickness. t_d for −173 °C-deposited CoFeB grown on TaB is about 0.28 ± 0.04 nm,

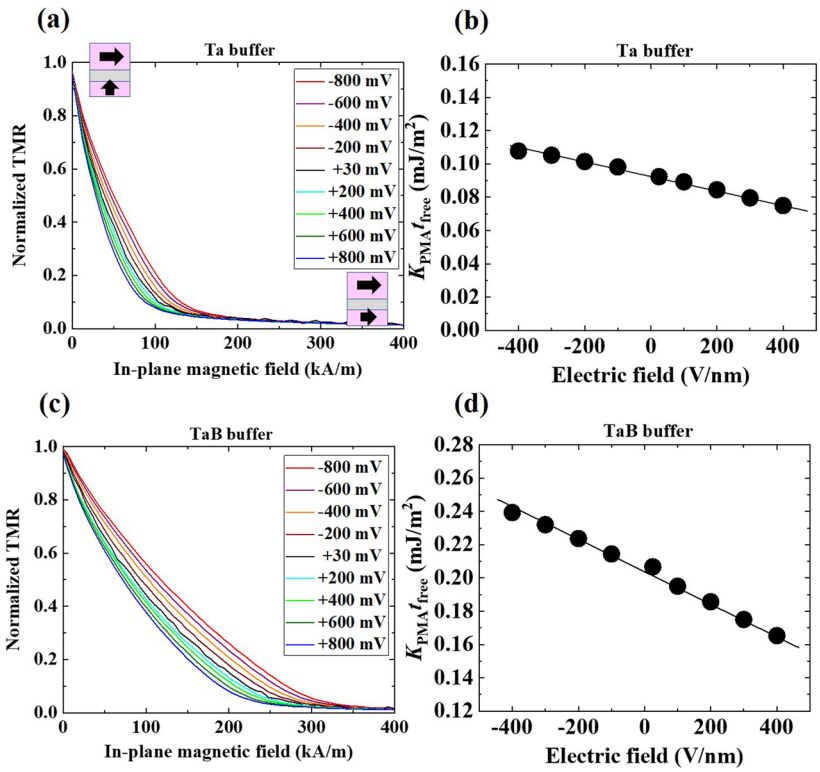

FIG. 2. Bias voltage dependence of normalized TMR curves measured under in-plane magnetic fields and the applied electric-field dependence of $K_{PMA}t_{free}$ for MTJs with a Ta buffer (a) and (b) and with a TaB buffer (c) and (d).

which is smaller than that of −173 °C-deposited CoFeB grown on a Ta buffer (0.45 ± 0.05 nm). A linear change in $K_{PMA}t_{free}$ is observed in both cases with the relation that electron accumulation (depletion) results in a decrease (an increase) in the PMA. The slope, i.e., the VCMA coefficient, is greater for the MTJ with the TaB buffer compared to that with the Ta buffer.

Figure 3 exhibits detailed comparisons of the saturation magnetization M_S, the half TMR ratio, $K_{PMA}t_{free}$, and the VCMA coefficient for the MTJs with Ta and TaB buffers prepared with post-annealing temperatures of T_{an} = 300 and 350 °C. In the case of the TaB buffer, the results for a CoFeB free layer deposited at room temperature (RT) are also shown (blue dots) in order to examine the influence of the cryogenic temperature deposition process. The values of M_S with T_{an} = 300 °C are almost the same for all the samples. On the other hand, with T_{an} = 350 °C, we can clearly see lower values of M_S for the MTJ with a Ta buffer and that with a TaB buffer and CoFeB deposited at RT compared to that with a TaB buffer and CoFeB deposited at −173 °C, of which the value remains at about 1.8 T. The MTJ with CoFeB deposited on the TaB buffer at −173 °C has a higher half TMR ratio when post-annealing is performed at T_{an} = 300 °C; however, with T_{an} = 350 °C, the half TMR ratio is almost the same for all the MTJs regardless of the buffer material and deposition temperature of the CoFeB layer. The type of buffer material and the deposition temperature of the CoFeB layer have more significant influences on $K_{PMA}t_{free}$ and the VCMA properties. The PMA for the MTJ with a TaB buffer is clearly higher than that with the Ta buffer. In the case of Ta buffer, we see a decrease in PMA at T_{an} = 350 °C; however, in the case of TaB buffer, the PMA remains high after annealing at this temperature. Making a comparison between different deposition temperatures, PMA for CoFeB deposited at RT exhibits a little higher PMA compared to that deposited at −173 °C. This tendency is opposite to that observed in the ultrathin CoFeB layer deposited on MgO reported in our previous work.[38] As for the VCMA, the highest VCMA coefficient of −105 ± 4 fJ/Vm is obtained for the MTJ with CoFeB deposited at −173 °C and post-annealed at T_{an} = 300 °C. Almost the same value is obtained with T_{an} = 350 °C. Meanwhile, the VCMA coefficient for the MTJ with the Ta buffer and CoFeB deposited at RT is reduced at T_{an} = 350 °C. This tendency is similar to that observed in the annealing temperature dependence of M_S.

B. Structural analysis

To throw some light on the observed differences in the PMA, TMR, and VCMA properties, we performed detailed microstructural characterization using STEM, NBED, and EDS. Figures 4(a)

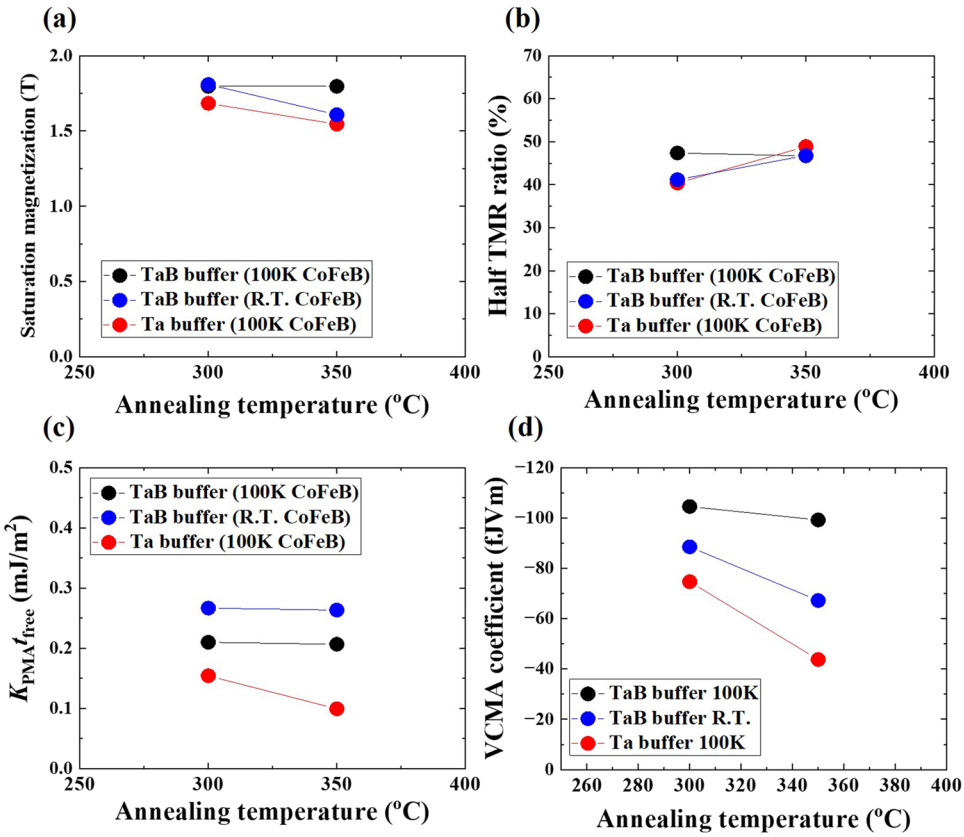

FIG. 3. Comparison of the annealing temperature dependence of (a) the saturation magnetization, (b) the half TMR ratio, (c) $K_{PMA}t_{free}$, and (d) the VCMA coefficient for MTJs with ultrathin CoFeB layers deposited at −173 °C on Ta or TaB buffers. For the TaB buffer, the results for a CoFeB free layer deposited at room temperature are also shown.

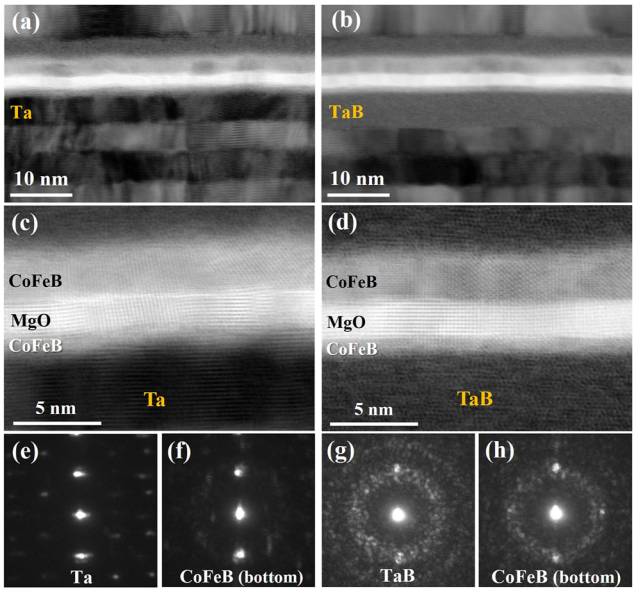

FIG. 4. Cross-sectional bright-field STEM images of the MTJ stack with (a), (c) a Ta buffer and (b), (d) a TaB buffer. (e)–(h) NBED patterns taken from (e) the Ta buffer layer, (f) the CoFeB layer grown on the Ta buffer, (g) the TaB buffer layer, and (h) the CoFeB layer grown on the TaB buffer.

and 4(b) show the low magnification bright field (BF)-STEM images for the MTJs with −173 °C-deposited CoFeB with the (a) Ta buffer and (b) TaB buffer, respectively. The post-annealing temperature was fixed at T_{an} = 350 °C in both cases. Large roughness at the Ta/CoFeB interface is seen, which leads to an increase in roughness even for the MgO tunneling barrier and the top CoFeB layers. Meanwhile, flatter interfaces are obtained through the whole multilayer structure for the case with the TaB buffer. Figures 4(c) and 4(d) display the high-resolution BF-STEM images focused around the MgO tunneling barrier for the MTJs with (c) the Ta buffer and (d) the TaB buffer, respectively. The polycrystalline structure of the Ta buffer is shown in Fig. 4(c). The NBED pattern in Fig. 4(e) clearly shows that the grains grow in the c-axis direction and rotate in the in-plane direction. In contrast, TaB contains an amorphous phase even after post-annealing at 350 °C as seen in the halo pattern of Fig. 4(g). Suppression of poly-crystallization even under the high annealing condition results in the flat TaB/CoFeB interface, which also leads to the flatter CoFeB/MgO interface. The preferred orientation of MgO(001) is obtained in both structures. As for the ultrathin CoFeB layer, partial crystallization can be seen close to the CoFeB/MgO interface in both cases; however, the NBED patterns are completely different. Figure 4(f) clearly confirms the crystallization of CoFeB(001) grown on the Ta buffer, while that grown on the TaB buffer contains an amorphous phase as revealed by the halo pattern in Fig. 4(h).

Figures 5(a) and 5(b) show the EDS line profiles (Co, Fe, Mg, O, Ta, and Ru) normal to the plane for MTJs with −173 °C-deposited CoFeB with (a) the Ta buffer and (b) the TaB buffer, respectively. Here, the boron concentration is not included. Most of the features are almost the same; however, we see a clear difference in the Ta distribution in the ultrathin CoFeB layer. For the case with the Ta buffer, we can see a broader tail in the Ta signal in the CoFeB layer even close to the CoFeB/MgO interface as indicated by the red arrow in Fig. 5(a). Meanwhile, the amplitude of the Ta signal in the CoFeB layer is clearly smaller for the case with the TaB buffer. Since the half widths of the Fe and Co profiles of the ultrathin CoFeB layer are almost the same in both structures, we can rule out the influence of film roughness at the Ta/CoFeB interface. These results suggest that the TaB buffer has higher post-annealing tolerance to Ta diffusion, resulting in the formation of a less-contaminated CoFeB/MgO interface. Since the Ta contamination at the CoFeB/MgO interface can cause a drastic reduction in the VCMA effect,[22] its suppression

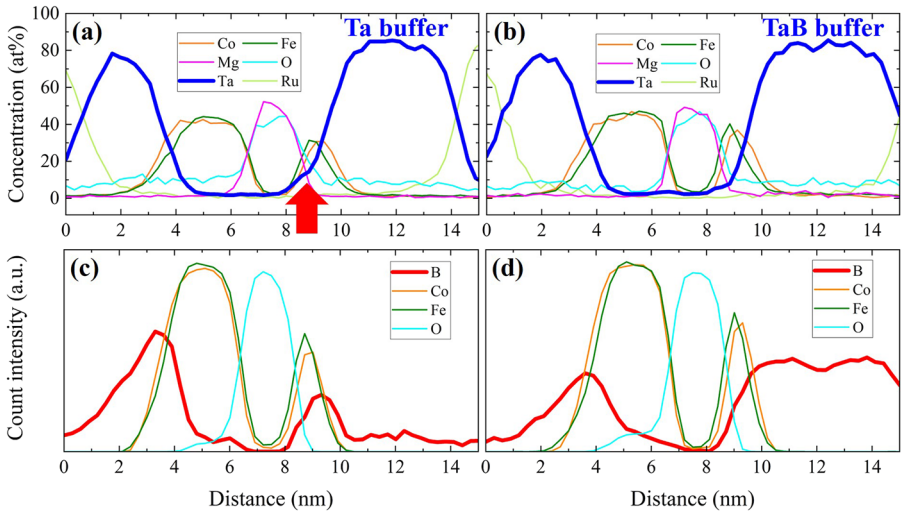

FIG. 5. EDS and EELS line profiles of the MTJs with (a), (c) a Ta buffer and (b), (d) a TaB buffer.

during the annealing process should play an important role in achieving the large VCMA effect.

We also performed EELS analysis (B, Co, Fe, and O) for the same samples to examine the elemental distribution especially focusing on boron as shown in Fig. 5(c) for the Ta buffer and Fig. 5(d) for the TaB buffer. In both cases, we can see the diffusion of boron from the CoFeB/MgO interface into the buffer layer, suggesting crystallization of CoFeB close to the interface with MgO after the annealing treatment. However, the boron concentration in the CoFeB layer is clearly higher in the MTJ with the TaB buffer, implying that the CoFeB layer contains an amorphous phase especially close to the TaB/CoFeB interface. This trend is consistent with the discussion of the NBED patterns [Fig. 4(h)].

We also performed cross-sectional STEM, NBED, EDS, and EELS analyses for the MTJ with CoFeB deposited at room temperature on the TaB buffer (not shown here); however, no significant differences were observed in the structural properties, such as the interfacial flatness, the NBED patterns, and the compositional profiles compared to those for the MTJ deposited at low temperatures. In our previous work, the low temperature deposition process was effective in reducing intermixing rather than improving the morphology when an ultrathin CoFeB layer was deposited on MgO.[38] Since the magnetic dead layer thickness of the RT-deposited CoFeB layer is a little larger (0.32 ± 0.03 nm) than that of the −173 °C-deposited one (0.28 ± 0.04 nm), we may obtain a less-intermixed interface even when growing CoFeB on a TaB buffer. To examine the effect of this on the VCMA properties, atomic scale chemical analysis, such as that provided by an atom probe method,[40] is required for future work.

The results obtained suggest that the combination of the TaB buffer and cryogenic temperature deposition can provide a flat and less-contaminated ultrathin CoFeB layer having clean interfaces with both the MgO tunneling barrier and the buffer layers. These features can be the dominant origin of the observed large VCMA effect. It is interesting that sufficient PMA and TMR can be obtained with partial crystallization of the CoFeB layer at the interface with MgO, although the amorphous phase of CoFeB is maintained by the high boron concentration even after annealing at 350 °C.

It should be noted that we observe a mismatch in the compositional distributions of Fe and Co at the CoFeB/MgO interface regardless of which buffer layer is used, i.e., the Fe concentration becomes unintentionally higher at the interface with MgO as shown

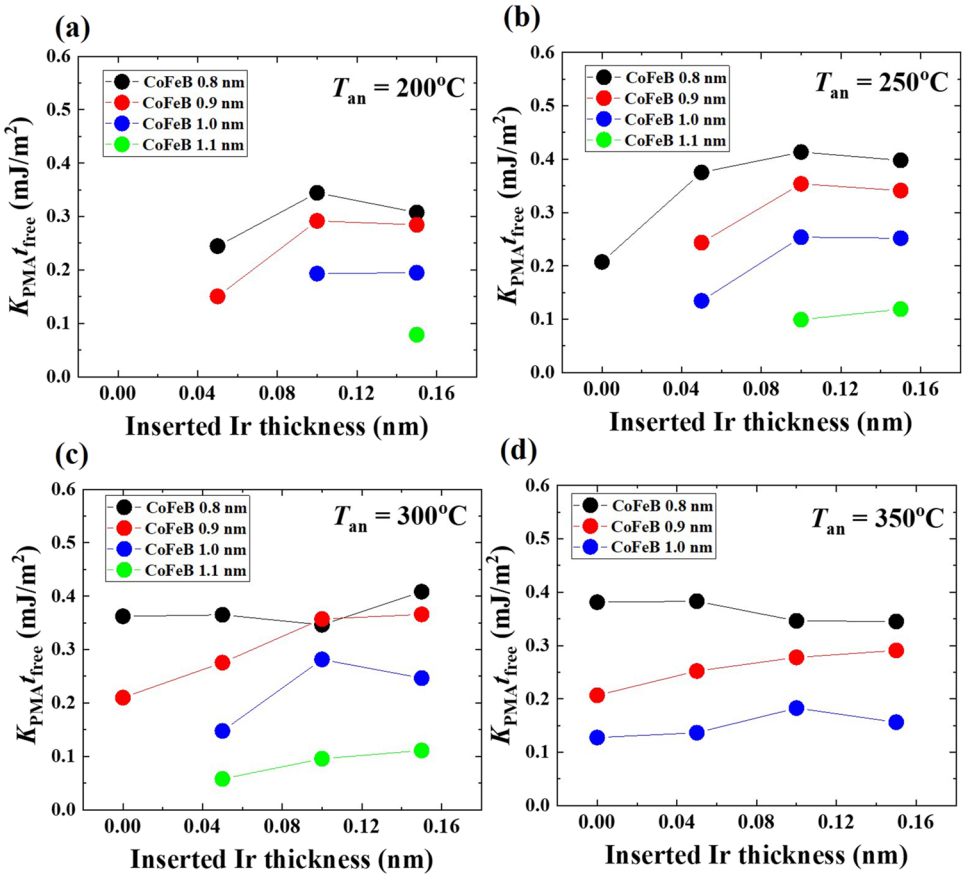

FIG. 6. The effect of inserting an Ir layer on the interfacial PMA. The Ir thickness dependence of $K_{PMA}t_{free}$ for an ultrathin CoFeB layer grown on a TaB buffer prepared at different post-annealing temperatures, T_{an}, of (a) 200 °C, (b) 250 °C, (c) 300 °C, and (d) 350 °C. The CoFeB layer was deposited at −173 °C, and its thickness, t_{CFB}, was varied from 0.8 to 1.1 nm.

in Fig. 5. A similar trend was observed at the CoFeB/MgO interface in our previous work.[29] Although an Fe-rich interface is effective in enhancing the interfacial PMA, it is not suitable for the VCMA because a Co-rich interface is preferable for improving the VCMA coefficient by Ir doping.[35] This can be prevented by the introduction of a CoFe termination layer as discussed in Sec. III C.

C. Optimization of the VCMA properties by introducing an Ir layer and a CoFe termination layer

Finally, based on the MTJ with the TaB buffer and the ultrathin CoFeB layer deposited at −173 °C, we attempted to optimize the VCMA properties by introducing a heavy metal Ir layer and a CoFe termination layer following the structural concept developed for fully epitaxial MTJs in our previous work.[34–36]

We first investigated the influence of direct insertion of an ultrathin Ir layer at the CoFeB/MgO interface, i.e., the CoFe termination layer has not yet been introduced. We confirmed that no clear structural difference was induced by the Ir insertion compared to the MTJ without the Ir insertion (see S1 of the supplementary material). Figure 6 shows the dependence of $K_{PMA}t_{free}$ on the thickness of the Ir layer for various annealing temperatures, T_{an}: (a) 200 °C, (b) 250 °C, (c) 300 °C, and (d) 350 °C. The CoFeB thickness, t_{CFB}, was varied from 0.8 to 1.1 nm. With the lower annealing temperatures, T_{an} < 250 °C, $K_{PMA}t_{free}$ tends to increase up to t_{Ir} = 0.1 nm and saturates at t_{Ir} > 0.1 nm. This tendency weakens at higher annealing temperatures as shown in Fig. 6(d). The observed trend can be understood as follows: with low temperature annealing at T_{an} < 250 °C, the intrinsic interfacial PMA for CoFeB/MgO is still small due to insufficient crystallization of the CoFeB(001) layer. However, the low annealing temperature keeps the Ir atoms close to the CoFeB/MgO interface, providing an enhancement in the interfacial PMA through proximity induced magnetism of the dispersed Ir with large spin–orbit interactions. Therefore, doping provided by the Ir layer has a dominant effect in the interfacial PMA when annealed at lower temperatures. Meanwhile, with T_{an} = 350 °C, CoFeB is partially crystallized close to the interface with MgO as discussed above and illustrated in Fig. 4, resulting in a higher intrinsic PMA at the CoFeB(001)/MgO interface. In contrast, the Ir atoms can diffuse deeply into the CoFeB layer, and then, the effect of the Ir doping becomes weaker (see S1 of the supplementary material).

Figure 7 shows the VCMA properties evaluated for the MTJs shown in Fig. 6. Compared to the TaB/CoFeB/MgO structure (−105 ± 4 fJ/Vm), the introduction of an ultrathin 0.05 nm thick Ir layer gives rise to a slight increase to −120 ± 3 fJ/Vm in the VCMA

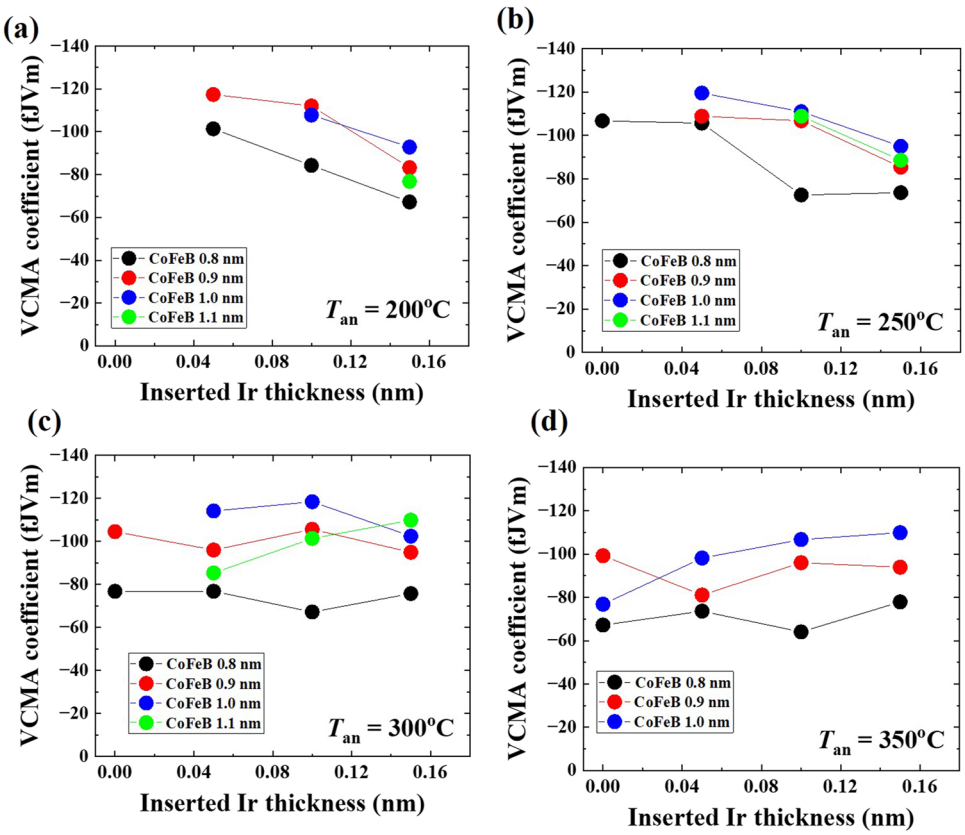

FIG. 7. The effect of inserting an Ir layer on the VCMA effect. The Ir thickness dependence of the VCMA coefficient for MTJs with an ultrathin CoFeB grown on a TaB buffer prepared at different post-annealing temperatures, T_{an}, of (a) 200 °C, (b) 250 °C, (c) 300 °C, and (d) 350 °C. t_{CFB} was varied from 0.8 to 1.1 nm.

coefficient when annealed at T_{an} < 250 °C. However, the VCMA coefficient tends to decrease with further increases in thickness of the Ir layer, indicating that we have the optimum Ir doping concentration to maximize the VCMA effect. With T_{an} = 350 °C, the dependence of the VCMA coefficient on the Ir thickness becomes weaker and the opposite trend is even observed, i.e., the VCMA coefficient increases with increasing Ir thickness for the case of t_{CFB} = 1.0 nm. With a 0.15 nm thick Ir layer, a VCMA coefficient of −110 ± 3 fJ/Vm was obtained. Due to the increase in the CoFeB thickness, the optimal Ir concentration condition at the CoFeB/MgO interface may shift to the thicker Ir thickness. The result implies that the thermal annealing tolerance can be improved by tuning the Ir distribution at the interface considering the diffusion process during annealing treatment, for example by controlling the thickness ratio between the CoFeB layer and the thin Ir layer as observed in this experiment. As for the TMR ratio, we observed a monotonic decrease by the Ir insertion. However, contrary to the case of epitaxial MTJs in our previous work,[35] the reduction rate is much smaller in the polycrystalline MTJs. For the optimized condition of VCMA effect, i.e., t_{Ir} = 0.05 nm, the reduction in TMR is almost negligible (see S2 of the supplementary material).

In fully epitaxial systems, the insertion of a CoFe termination layer was effective in enhancing the VCMA effect in the Fe/Ir/MgO structure.[35] The first-principles calculations revealed that the high VCMA effect in the Ir-doped Fe system mainly comes from an electric-field induced modification of the spin-conserving term of the majority spin 5*d* states of Ir. Interestingly, Ir atoms located in the second layer from the interface can show a larger VCMA effect than that in the topmost surface layer adjacent to the MgO. Furthermore, its effect can be enhanced by the introduction of a CoFe termination layer. Following this concept, the PMA and VCMA properties were investigated in the TaB/CoFeB(0.8 nm)/Ir(t_{Ir})/CoFe(0.1 nm)/MgO structures. Here, both the CoFeB and CoFe layers were deposited at −173 °C. Figures 8(a) and 8(b) show the examples of the bias voltage dependence of normalized TMR curves and the applied electric field dependence of $K_{PMA}t_{free}$ observed in the MTJ with the free layer structure of CoFeB(0.8 nm)/Ir(0.05 nm)/CoFe(0.1 nm). With the post-annealing temperature T_{an} = 200 °C, a high VCMA coefficient of −138 ± 3 fJ/Vm is achieved. Figures 8(c) and 8(d) show the Ir thickness dependence of (c) $K_{PMA}t_{free}$ and (d) the VCMA coefficient for MTJs with the free layer structure of CoFeB(0.8 nm)/Ir(t_{Ir})/CoFe(0.1 nm) prepared with different

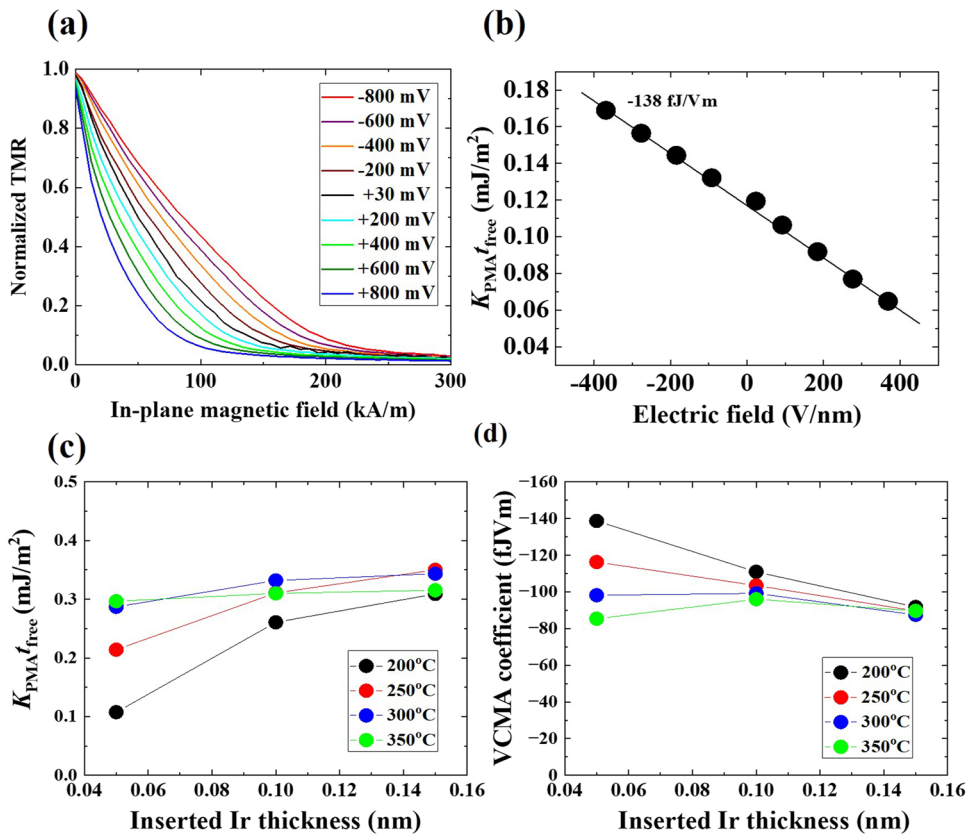

FIG. 8. Optimization of the VCMA effect by inserting an Ir layer and a CoFe termination layer. Example of (a) bias voltage dependence of normalized TMR curves and (b) applied electric-field dependence of $K_{PMA}t_{free}$ observed in a TaB/CoFeB(0.8 nm)/Ir(0.05 nm)/CoFe(0.1 nm)/MgO/CoFeB(3 nm) structure post-annealed at 200 °C. The Ir thickness dependence of (c) $K_{PMA}t_{free}$ and (d) the VCMA coefficient prepared at different post-annealing temperatures observed in the free layer structure of CoFeB(0.8 nm)/Ir(t_{Ir} nm)/CoFe(0.1 nm).

post-annealing temperatures. Similar to the case without the CoFe termination layer, we observe a clear increase in PMA with the Ir layer at low annealing temperatures; however, its dependence becomes weaker under higher temperature annealing. The VCMA coefficient also shows a strong dependence on the Ir thickness with T_{an} = 200 °C. The maximum VCMA coefficient of −138 ± 3 fJ/Vm obtained at t_{Ir} = 0.05 nm becomes about −92 ± 3 fJ/Vm at t_{Ir} = 0.15 nm. At the higher annealing temperatures, the VCMA coefficient becomes smaller and tends to be independent of the Ir layer thickness. Further improvement in the annealing tolerance can be expected by adjusting the ratio of the thicknesses of the CoFeB and Ir layers as discussed above and also by placing the Ir layer far from the CoFeB/MgO interface, such as using ultrathin Ir buffer or middle Ir insertion layers.

IV. CONCLUSIONS

We investigated the influence of the buffer material and cryogenic temperature deposition of an ultrathin CoFeB layer on the TMR, PMA, and VCMA properties in polycrystalline MTJs with a bottom free layer prepared by the mass-production sputtering system. We found that the TaB buffer can realize the ideal flat and less-contaminated CoFeB/MgO interface through the stable amorphous phase and suppression of Ta diffusion into CoFeB. Furthermore, the introduction of a cryogenic temperature deposition process for the ultrathin CoFeB layer on the TaB buffer had a strong impact on improving the VCMA coefficient. By combining this with interface engineering employing an Ir doping layer and a CoFe termination layer, a high VCMA coefficient of −138 ± 3 fJ/Vm was successfully achieved. The developed MTJ fabrication process for mass production is expected to greatly contribute to the development of high-performance VC-MRAMs.

SUPPLEMENTARY MATERIAL

See the supplementary material for the Ir insertion effect on multilayer structure and TMR properties.

ACKNOWLEDGMENTS

This work was partly based on results obtained from a project, JPNP16007, commissioned by the New Energy and Industrial Technology Development Organization (NEDO), Japan, and JSPS KAKENHI (S) under Grant No. JP20H05666. The authors thank Y. Kageyama, L. Sakai, K. Hiraga, K. Ohba, Y. Higo, and M. Hosomi of Sony Semiconductor Solutions Corporation for their fruitful discussions.

AUTHOR DECLARATIONS

Conflict of Interest

The authors have no conflicts to disclose.

Author Contributions

Takayuki Nozaki: Conceptualization (lead); Data curation (lead); Formal analysis (lead); Funding acquisition (supporting); Investigation (lead); Writing – original draft (lead). **Tomohiro Ichinose**: Methodology (supporting); Writing – review & editing (supporting). **Jun Uzuhashi**: Data curation (supporting); Investigation (supporting); Methodology (supporting); Writing – review & editing (supporting). **Tatsuya Yamamoto**: Methodology (supporting); Writing – review & editing (supporting). **Makoto Konoto**: Methodology (supporting); Writing – review & editing (supporting). **Kay Yakushiji**: Methodology (supporting); Writing – review & editing (supporting). **Tadakatsu Ohkubo**: Investigation (supporting); Methodology (supporting); Writing – review & editing (supporting). **Shinji Yuasa**: Funding acquisition (lead); Project administration (lead); Writing – review & editing (supporting).

DATA AVAILABILITY

The data that support the findings of this study are available from the corresponding author upon reasonable request.

REFERENCES

[1] S. Yuasa, T. Nagahama, A. Fukushima, Y. Suzuki, and K. Ando, Nat. Mater. **3**, 868 (2004).
[2] S. S. P. Parkin, C. Kaiser, A. Panchula, P. M. Rice, B. Hughes, M. Samant, and S. H. Yang, Nat. Mater. **3**, 862 (2004).
[3] C. Safranski, G. Hu, J. Z. Sun, P. Hashemi, S. L. Brown, L. Buzi *et al.*, in *2022 IEEE Symposium on VLSI Technology and Circuits (VLSI Technology and Circuits)* (IEEE, 2022), p. 288.
[4] T. Nozaki, T. Yamamoto, S. Miwa, M. Tsujikawa, M. Shirai, S. Yuasa, and Y. Suzuki, Micromachines **10**, 327 (2019).
[5] S. Miwa, M. Suzuki, M. Tsujikawa, T. Nozaki, T. Nakamura, M. Shirai *et al.*, J. Phys. D: Appl. Phys. **52**, 063001 (2019).
[6] P. K. Amiri, J. G. Alzate, X. Q. Cai, F. Ebrahimi, Q. Hu, K. Wong *et al.*, IEEE Trans. Magn. **51**, 3401507 (2015).
[7] M. Weisheit, S. Fähler, A. Marty, Y. Souche, C. Poinsignon, and D. Givord, Science **315**, 349 (2007).
[8] T. Maruyama, Y. Shiota, T. Nozaki, K. Ohta, N. Toda, M. Mizuguchi *et al.*, Nat. Nanotechnol. **4**, 158 (2009).
[9] T. Nozaki, Y. Shiota, M. Shiraishi, T. Shinjo, and Y. Suzuki, Appl. Phys. Lett. **96**, 022506 (2010).
[10] C. G. Duan, J. P. Velev, R. F. Sabirianov, Z. Zhu, J. Chu, S. S. Jaswal, and E. Y. Tsymbal, Phys. Rev. Lett. **101**, 137201 (2008).
[11] K. Nakamura, R. Shimabukuro, Y. Fujiwara, T. Akiyama, T. Ito, and A. J. Freeman, Phys. Rev. Lett. **102**, 187201 (2009).
[12] M. Tsujikawa and T. Oda, Phys. Rev. Lett. **102**, 247203 (2009).
[13] S. Miwa, M. Suzuki, M. Tsujikawa, K. Matsuda, T. Nozaki, K. Tanaka *et al.*, Nat. Commun. **8**, 15848 (2017).
[14] Y. Shiota, T. Nozaki, F. Bonell, S. Murakami, T. Shinjo, and Y. Suzuki, Nat. Mater. **11**, 39 (2012).
[15] S. Kanai, M. Yamanouchi, S. Ikeda, Y. Nakatani, F. Matsukura, and H. Ohno, Appl. Phys. Lett. **101**, 122403 (2012).
[16] C. Grezes, H. Lee, A. Lee, S. Wang, F. Ebrahimi, X. Li *et al.*, IEEE Magn. Lett. **8**, 3102705 (2016).
[17] T. Yamamoto, R. Matsumoto, T. Nozaki, H. Imamura, and S. Yuasa, J. Magn. Magn. Mater. **560**, 169637 (2022).
[18] Y. Shao, V. Lopez-Dominguez, N. Davila, Q. Sun, N. Kioussis, J. A. Katine *et al.*, Commun. Mater. **3**, 87 (2022).
[19] S. Kanai, F. Matsukura, and H. Ohno, Appl. Phys. Lett. **108**, 192406 (2016).
[20] C. Grezes, F. Ebrahimi, J. G. Alzate, X. Cai, J. A. Katine, J. Langer *et al.*, Appl. Phys. Lett. **108**, 012403 (2016).
[21] Y. Shiota, T. Nozaki, S. Tamaru, K. Yakushiji, H. Kubota, A. Fukushima *et al.*, Appl. Phys. Express **9**, 013001 (2016).
[22] X. Li, K. Fitzell, D. Wu, C. T. Karaba, A. Buditama, G. Yu *et al.*, Appl. Phys. Lett. **110**, 052401 (2017).

[23]T. Nozaki, T. Nozaki, H. Onoda, H. Nakayama, T. Ichinose, T. Yamamoto *et al.*, APL Mater. **10**, 081103 (2022).
[24]X. Li, T. Sasaki, C. Grezes, D. Wu, K. Wong, C. Bi *et al.*, Nano Lett. **19**, 8621 (2019).
[25]S. Miwa, J. Fujimoto, P. Risius, K. Nawaoka, M. Goto, and Y. Suzuki, Phys. Rev. X **7**, 031018 (2017).
[26]W. Skowroński, T. Nozaki, D. D. Lam, Y. Shiota, K. Yakushiji, H. Kubota *et al.*, Phys. Rev. B **91**, 184410 (2015).
[27]W. Skowroński, T. Nozaki, Y. Shiota, S. Tamaru, K. Yakushiji, H. Kubota *et al.*, Appl. Phys. Exp. **8**, 053003 (2015).
[28]T. Nozaki, A. Kozioł-Rachwał, W. Skowroński, V. Zayets, Y. Shiota, S. Tamaru *et al.*, Phys. Rev. Appl. **5**, 044006 (2016).
[29]T. Yamamoto, T. Nozaki, K. Yakushiji, S. Tamaru, H. Kubota, A. Fukushima, and S. Yuasa, Acta Mater. **216**, 117097 (2021).
[30]X. Li, G. Yu, H. Wu, P. V. Ong, K. Wong, Q. Hu *et al.*, Appl. Phys. Lett. **107**, 142403 (2015).
[31]Z. Wen, H. Sukegawa, T. Seki, T. Kubota, K. Takanashi, and S. Mitani, Sci. Rep. **7**, 45026 (2017).
[32]D. Chien, X. Li, K. Wong, M. A. Zurbuchen, S. Robbennolt, G. Yu *et al.*, Appl. Phys. Lett. **108**, 112402 (2016).
[33]H. Onoda, T. Nozaki, S. Tamaru, T. Nozaki, and S. Yuasa, Phys. Rev. Mater. **6**, 104406 (2022).
[34]T. Nozaki, A. Kozioł-Rachwał, M. Tsujikawa, Y. Shiota, X. Xu, T. Ohkubo *et al.*, NPG Asia Mater. **9**, e451 (2017).
[35]T. Nozaki, M. Endo, M. Tsujikawa, T. Yamamoto, T. Nozaki, M. Konoto *et al.*, APL Mater. **8**, 011108 (2020).
[36]T. Nozaki, T. Nozaki, T. Yamamoto, M. Konoto, A. Sugihara, K. Yakushiji, and S. Yuasa, Appl. Phys. Lett. **121**, 172401 (2022).
[37]K. Nakamura, T. Nomura, A. M. Pradipto, K. Nawa, T. Akiyama, and T. Ito, J. Magn. Magn. Mater. **429**, 214 (2017).
[38]T. Ichinose, T. Yamamoto, T. Nozaki, K. Yakushiji, S. Tamaru, M. Konoto, and S. Yuasa, ACS Appl. Electron. Mater. **5**, 2178 (2023).
[39]A. Sugihara, T. Ichinose, S. Tamaru, T. Yamamoto, M. Konoto, T. Nozaki, and S. Yuasa, Appl. Phys. Express **16**, 023003 (2023).
[40]Y. K. Takahashi, N. Hase, M. Kodzuka, A. Itoh, T. Koganezawa, T. Furubayashi *et al.*, J. Appl. Phys. **113**, 223901 (2013).